Microstructure and Local Brittle Zone Phenomena in High-Strength Low-Alloy Steel Welds

B.C. KIM, S. LEE, N.J. KIM, and D.Y. LEE

This study is concerned with a correlation between the microstructure and the local brittle zone (LBZ) phenomena in high-strength low-alloy (HSLA) steel welds. The influence of the LBZ on toughness was investigated by means of simulated heat-affected zone (HAZ) tests as well as welded joint tests. Micromechanical processes involved in microvoid and cleavage microcrack formation were also identified using notched round tensile tests and subsequent scanning electron microscopy (SEM) analyses. The LBZ in the HAZ of a multipass welded joint is the intercritically reheated coarse-grained HAZ whose properties are strongly influenced by metallurgical factors such as an effective grain size and high-carbon martensitic islands. The experimental results indicated that Charpy energy was found to decrease monotonically with increasing the amount of martensitic islands, confirming that the martensitic island is the major microstructural factor controlling the HAZ toughness. In addition, microvoids and microcracks were found to initiate at the interface between the martensitic island and the ferrite matrix, thereby causing the reduction in toughness. These findings suggest that the LBZ phenomena in the coarse-grained HAZ can be explained by the morphology and the amount of martensitic islands.

I. INTRODUCTION

RECENTLY, very low toughness values have been noticed in the heat-affected zones (HAZ's) of high-strength low-alloy (HSLA) steels welded with multipass submerged arc welding (SAW) procedures.[1–6] Metallographic analyses of HSLA steel welds reveal significantly different regions in HAZ microstructures. For example, in single-pass welds, there are four characteristic regions in the HAZ determined by the peak temperature, to which the region was exposed during the weld thermal cycle:[5,7] a coarse-grained region, a fine-grained region, an intercritical region, and a subcritical region. In multipass welds, these regions undergo multiple thermal cycles, resulting in inhomogeneous and complicated microstructures. An idealized sketch of a heat-affected multipass weld is shown in Figure 1. The coarse-grained region can be roughly categorized into four zones according to the reheating temperature as follows: (a) a subcritically reheated coarse-grained zone (SRCG HAZ), the zone reheated below Ac_1, (b) an intercritically reheated coarse-grained zone (ICRCG HAZ), the zone reheated between Ac_1 and Ac_3, (c) a supercritically reheated coarse-grained zone (SCRCG HAZ), the zone reheated above Ac_3 and below about 1200 °C, and (d) an unaltered coarse-grained zone (UACG HAZ), the zone that is not reheated or reheated above 1200 °C.

Although many studies have been conducted on HSLA steel welds, few reports are available on the factors that govern the toughness of the welded joints. It is now generally accepted that the coarse-grained region has the lowest toughness. This local brittle zone (LBZ) becomes a serious problem since the low-temperature toughness is severely reduced due to the presence of the unfavorable microstructural features in the LBZ, such as large prior austenite grain size, upper bainite, martensitic islands, and microalloy precipitates.[3–8] Among the above microstructural features in the coarse-grained HAZ, the martensitic island is the main factor causing deterioration of toughness because of its high hardness and crack susceptibility,[5,6,9] although the relative ranking of the microstructural features depends on the chemical compositions and the local thermal cycles including post-weld heat treatments. The present work describes the specific roles of the microstructural factors, such as martensitic islands, in the process of microvoid and microcrack initiation in a 500 MPa class HSLA steel. Specifically, by examining the initiation of microvoids and microcracks in sectioned tensile specimens, the micromechanism of fracture processes is identified and related to the observed Charpy test results.

II. EXPERIMENTAL

A. *Material and Welding*

The material used in this study is a 44-mm-thick plate of a normalized BS 4360 Gr.50D steel. This is a high-strength grade steel with a tensile strength of about 500 MPa, whose chemical composition is 0.13C-0.4Si - 1.43Mn - 0.019P - 0.001S - 0.065Al - 0.3Cu - 0.22Ni-0.017Ti-0.021Nb. Welding was done by the tandem-electrode SAW process under the conditions shown in Table I. The heat input was 50 kJ/cm, which is typical for the fabrication welding of offshore platform constructions. A K-groove weld was adopted for testing a welded joint.

B. *Weld Simulation*

Weld simulation tests were conducted for the systematic investigation of the LBZ and its effect on toughness. The thermal cycle of the weld simulation is characterized

B.C. KIM, Research Assistant, S. LEE, Assistant Professor, N.J. KIM, Associate Professor, and D.Y. LEE, Associate Professor, are with the Department of Materials Science and Engineering, Pohang Institute of Science and Technology, Pohang 790, Korea.

Manuscript submitted August 30, 1989.

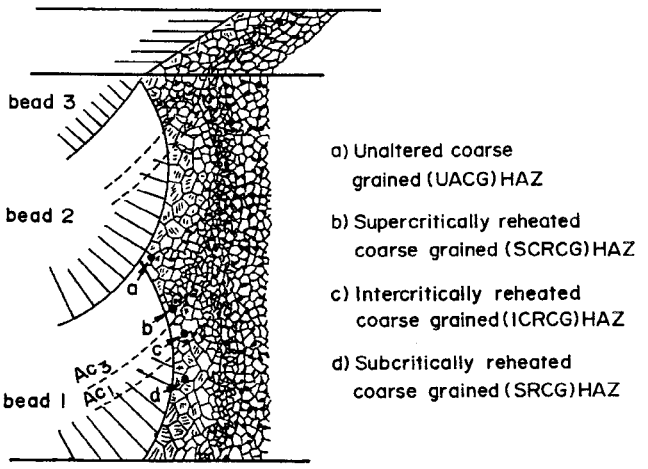

Fig. 1—Schematic diagram of a heat-affected multipass weld.

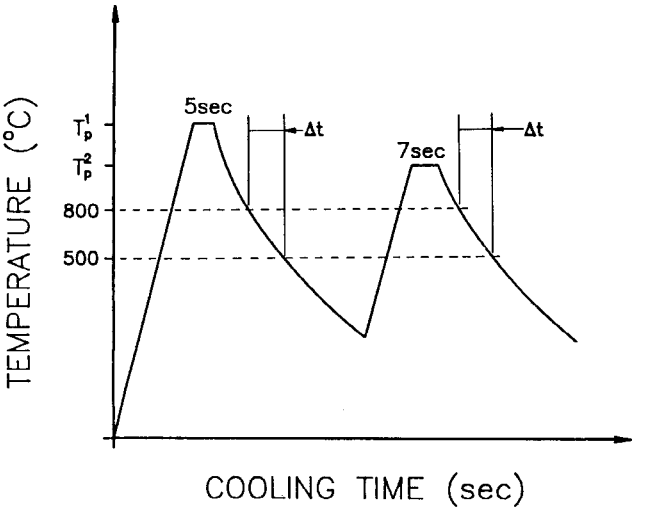

Fig. 2—Schematic diagram of a thermal simulation cycle.

by the peak temperature (T_p) and the cooling time from 800 °C to 500 °C ($\Delta t_{8/5}$). The thermal cycle used is shown schematically in Figure 2. After reaching the first peak temperature (T_p^1) of 1350 °C and a resting time of about 5 ~ 10 seconds, the specimens were cooled down with a $\Delta t_{8/5}$ of 20, 42, and 60 seconds. The cooling rate of 42 seconds is approximately equivalent to that of a SAW of a 44-mm-thick plate with a heat input of 50 kJ/cm.[10] The peak temperature of the second thermal cycle (T_p^2) was varied between 600 °C and 1200 °C for simulating the thermal cycle due to the second weld bead.

C. *Mechanical Testing*

The orientations of test specimens are illustrated in Figure 3(a). The crack tip opening displacement (CTOD) tests, which are commonly used to evaluate the fracture toughness of steel welds,[4-7,11] were carried out using single-notch three-point bend specimens with a deep crack (crack length to depth ratio, $a/w \approx 0.5$) in accordance with BS 5762.[12] By locating the crack tip in a specific region of the weldment, *e.g.*, the HAZ, the toughness of that region was characterized. A K-groove weld joint was used to achieve a straight HAZ because of the small size and irregular shape of the HAZ region. A validation check for the weldment specimens was made using metallographic sectioning technique after testing whether the crack tip placement requirements had been met. Charpy impact tests were also conducted on the welded joint. The Charpy V-notch specimens with *T-L* orientation were machined from the oversized Charpy blanks after thermal simulation treatments and were then tested at the temperature range from −80 °C to −10 °C.

To investigate the micromechanism of fracture under the triaxial stress conditions, tensile tests and subsequent metallographic analyses were conducted using circumferentially notched tensile specimens[13,14] whose shape and dimensions are illustrated in Figure 3(b). The specimens were pulled at a crosshead speed of 1.27 mm/min (0.05 in./min) initially and 0.51 mm/min (0.02 in./min) subsequent to yielding. The carbon evaporated grid was used to facilitate the measurement of local strains and strain gradients at various points along the specimen's axis. The plastic strain at a distance z measured from the point of minimum radius can be obtained from the relation $\varepsilon_z = 2 \ln (D_0/D_z)$, where D_0 and D_z are the initial

Table I. Welding Conditions

Welding process	Submerged arc welding (tandem)
Welding position	flat
Welding current	600 A
Arc voltage	30 V
Welding speed	43 cm/min
Preheating temperature	200 °C (max.)
Heat input	50 kJ/cm
Post weld heat treatment	none

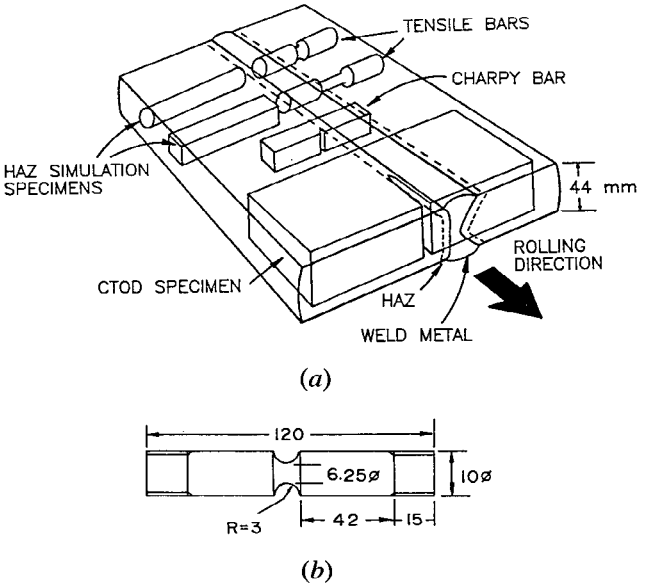

Fig. 3—(*a*) Sketch illustrating the orientations of the various specimens used. (*b*) The shape and dimensions of a circumferentially notched tensile specimen (unit, mm).

and instantaneous diameters, respectively. In this case, the strain is considered to be an appropriate parameter to relate to the average damage in the interior of the specimen.

D. *Microscopy*

The fracture surfaces of a number of fractured specimens were examined by scanning electron microscopy (SEM). Fractured tensile halves were first nickel-plated to avoid rounding during polishing and then sectioned longitudinally and mounted. These mounted specimens were polished and specially etched by using a two-stage electrolytic etching technique[15,16] to reveal martensitic islands.

Transmission electron microscopy (TEM) was extensively employed to characterize and identify the presence of retained austenite, twinned martensite, cementite, and other microstructural features. The thin foils were prepared from the fractured Charpy specimens. Final electropolishing was performed using an automatic twin-jet electropolisher using a solution of 50 ml perchloric acid and 50 ml acetic acid.

III. RESULTS

A. *Fracture Properties*

Figures 4 and 5 show, respectively, the results of CTOD tests and Charpy impact tests for the welded structures, *i.e.*, coarse-grained HAZ, subcritical HAZ, and base metal, obtained over the test temperature range from −80 °C to −10 °C. The variation of CTOD values with the test temperature range is similar to that of Charpy impact energies. The coarse-grained zone exhibits the lowest CTOD values, indicating that this zone is the LBZ in the HSLA steel welds.

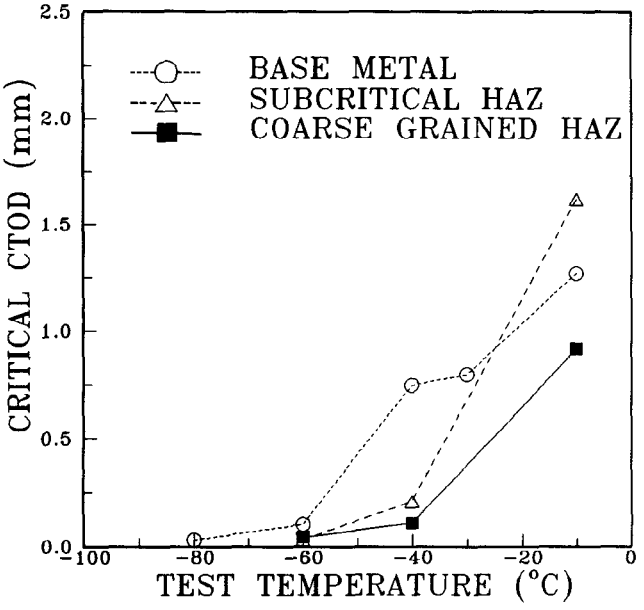

Fig. 4—CTOD values of base metal and HAZ's as a function of test temperature.

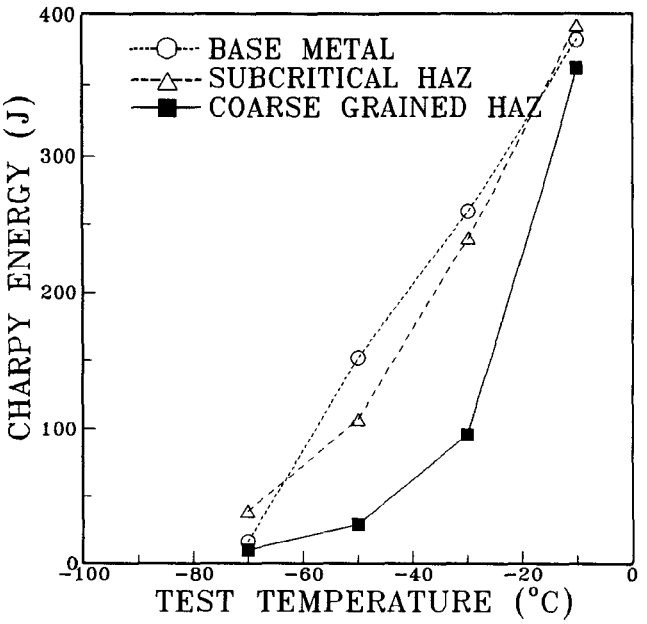

Fig. 5—Charpy impact energies of base metal and HAZ's as a function of test temperature.

The effect of the first thermal cycle on Charpy energy values for the simulated HAZ is shown in Figure 6. After applying the first thermal cycle with peak temperatures between 900 °C and 1350 °C, the second thermal cycle with a peak temperature of 800 °C was applied. The Charpy energy decreases steadily with increasing the T_p^1 in both the single and double simulation conditions. Slightly lower toughness values are found for the specimens subjected to the double thermal cycle.

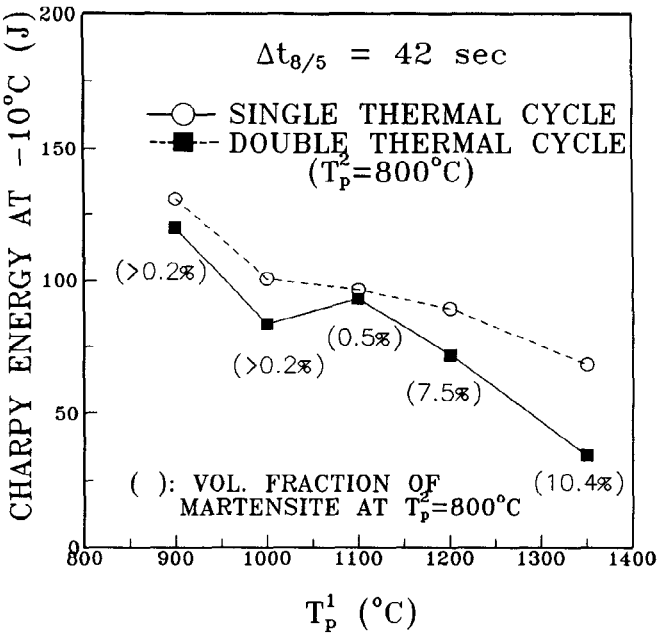

Fig. 6—Charpy impact energies *vs* the first peak temperature (T_p^1). Parentheses indicate the volume fraction of martensitic islands in the Charpy specimens subjected to the double thermal cycles (T_p^2 = 800 °C).

The results of Charpy tests in the simulated coarse-grained HAZ are shown in Figure 7. The coarse-grained HAZ exhibits low Charpy impact energies in two cases. The first is the one simulated by a single thermal cycle with a peak temperature of 1350 °C (UACG HAZ), and the second is the one simulated by double thermal cycles with T_p^2 in the range of 750 °C to 800 °C (ICRCG HAZ). The influence of cooling rate, $\Delta t_{8/5}$, on the Charpy toughness is not significant for this simulated coarse-grained HAZ.

Figure 8 shows the Charpy impact test results conducted over the test temperature range from −80 °C to −10 °C for the simulated UACG HAZ and ICRCG HAZ. The lower shelf impact energies do not differ substantially, whereas the upper shelf energies of the UACG HAZ are much higher than those of the ICRCG HAZ microstructures. It is also found that the ICRCG HAZ exhibits the lowest impact energy.

B. *Microstructure*

The grain sizes in the simulated HAZ are shown in Table II, along with other microstructural parameters. The grain sizes of the welded joint were quite similar to those of the simulated HAZ. The microstructure subjected to the thermal cycle with T_p^1 of 1350 °C is characterized by the coarse prior austenite grain sizes, as shown in Figures 9(a) and (b). Unaltered coarse-grained HAZ and ICRCG HAZ exhibit coarse-grained microstructures mainly composed of upper bainite. Equiaxed ferrite often located at former austenite grain boundaries, martensite, and lower bainite are also observed. These microstructures are so complicated that electron microscope analyses are required for identification of each constituent.

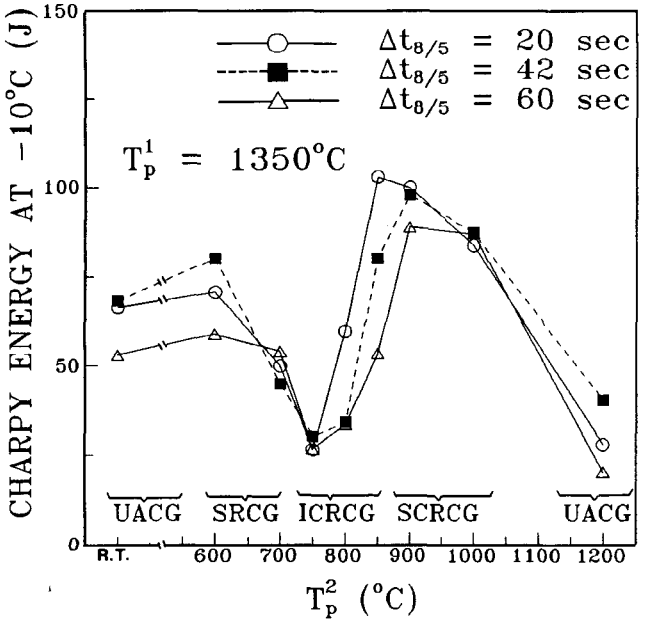

Fig. 7—Charpy impact energies *vs* the peak temperature of the second thermal cycle (T_p^2), showing two local brittle zones, UACG HAZ and ICRCG HAZ.

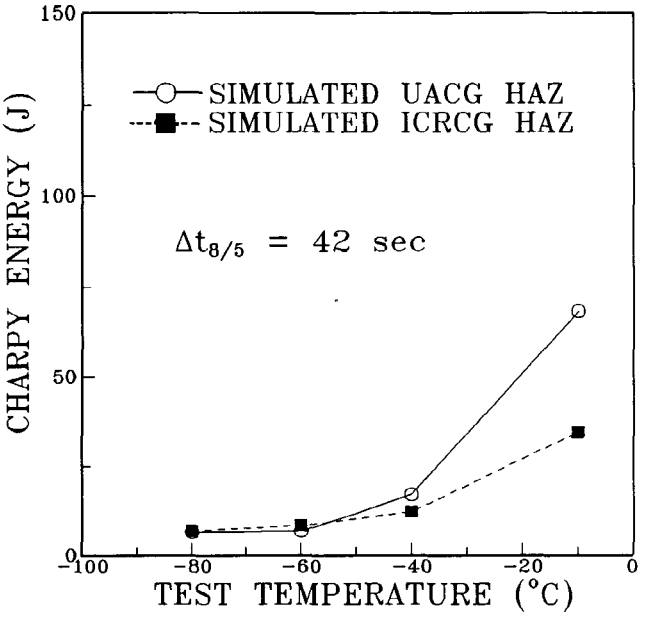

Fig. 8—Charpy impact energies *vs* test temperature for the UACG HAZ and ICRCG HAZ.

Transmission electron micrographs indicated that the ICRCG HAZ consists mainly of upper bainite, as shown in Figure 10. Figure 11(a) shows carbides along the bainite lath boundaries. A detailed electron microscopic analysis showed that these carbides are Fe_3C.

The ICRCG HAZ also contains a considerable amount of high-carbon martensitic islands and equiaxed ferrite in the coarse-grained bainite microstructure. The martensitic island is a dual-phase microstructure formed in the coarse-grained HAZ when the thermal cycle of a subsequent weld pass has a peak temperature in the intercritical two-phase (α + γ) region.[9,17] Upon cooling from

Table II. Microstructural Factors of the Simulated HAZ

1st Peak Temperature, T_p^1 (°C)	2nd Peak Temperature, T_p^2 (°C)	Prior Austenite Grain Size (μm)	Ferrite Grain Size (μm)	Volume Fraction of Martensitic Island (Pct)
1350	—	49	—	7.4
	1200	49	—	8.2
	1000	49	—	<0.2
	800	49	—	10.4
1200	—	41	—	6.5
	800	41	—	7.5
1100	—	30	8.7	<0.2
	800	30	8.7	0.5
1000	—	—	8.1	<0.2
	800	—	8.1	<0.2
900	—	—	7.6	<0.2
	800	—	7.6	<0.2

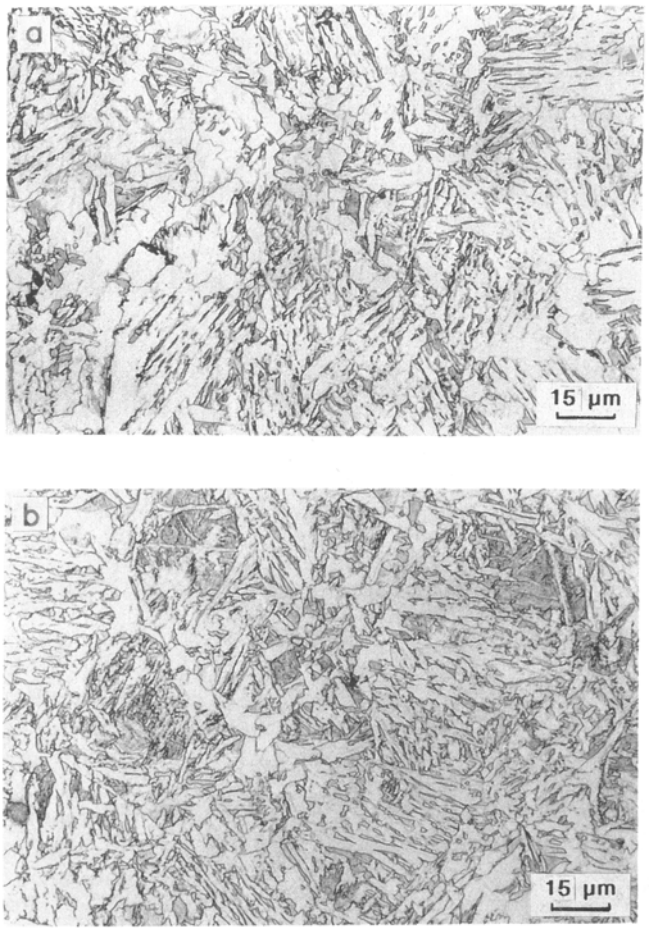

Fig. 9—Optical microstructures of (*a*) the simulated UACG HAZ and (*b*) the simulated ICRCG HAZ (T_p^2 = 1350 °C).

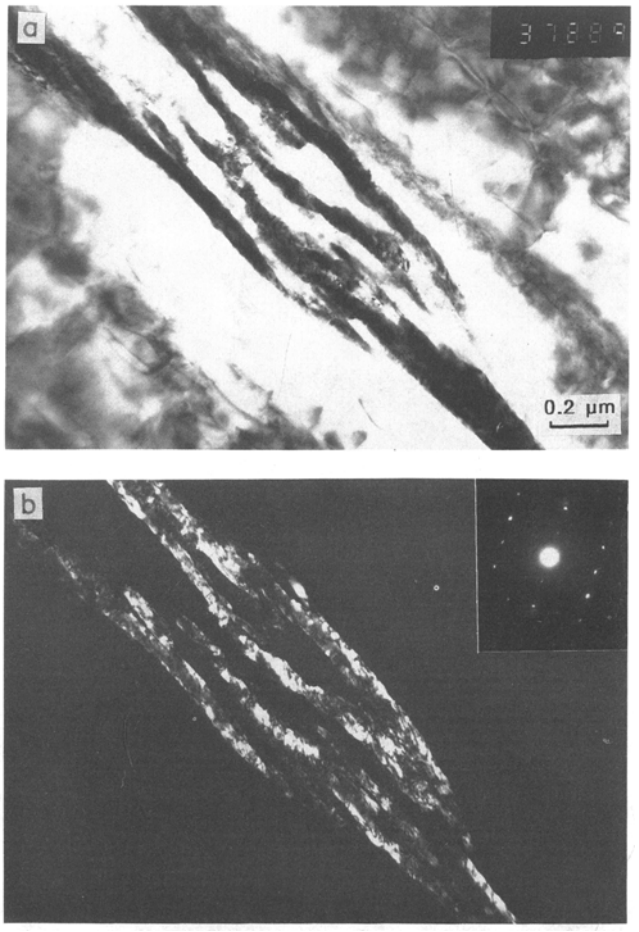

Fig. 11—Transmission electron micrographs of the simulated ICRCG HAZ, showing the typical upper bainite microstructure: (*a*) bright-field image and (*b*) dark-field image of discontinuous cementite films at bainite lath boundary.

the intercritical temperature, the austenite is stabilized to room temperature or transforms to martensite or other diffusional products. The morphology of martensite is basically dislocated lath type, and the presence of films of retained austenite was observed between the martensite laths. The bright- and dark-field images from the (002) retained austenite are shown in Figures 12(a) and (b). These results support that retained austenite exists in the martensitic islands, although the amount of retained austenite is quite small. Such a dual-phase microstructure is also called a "martensite-austenite (M-A) constituent" in the literature.[2,7,18] A small amount of twinned martensite was also observed. Figure 13 is the bright-field image of twinned martensites confirmed by using a {100} twin-related martensite spot.

Fig. 10—Transmission electron micrograph of the simulated ICRCG HAZ which consists of upper bainite, martensite, and ferrite.

When the specimens were specially etched using a two-stage electrolytic etching technique, martensitic islands were revealed in the coarse-grained bainite microstructures. In the intercritical region, austenite nucleates and grows preferentially along the bainite lath boundaries and the prior austenite grain boundaries.[6,9,19] Thus, upon cooling, some part of the austenite is transformed into martensitic islands with the morphology of elongated stringer type, reflecting the morphology of austenite prior to transformation. A relatively small amount of blocky-type martensitic islands is also observed.

A careful analysis of the volume fraction of martensitic islands provides an explanation for the variation of the Charpy impact test results. Table II shows the volume fraction evaluated by the image processing method for the simulated HAZ. The amount of martensitic islands tends to increase with T_p^1 (Figure 6). When T_p^1 is fixed at 1350 °C and the second peak temperature (T_p^2)

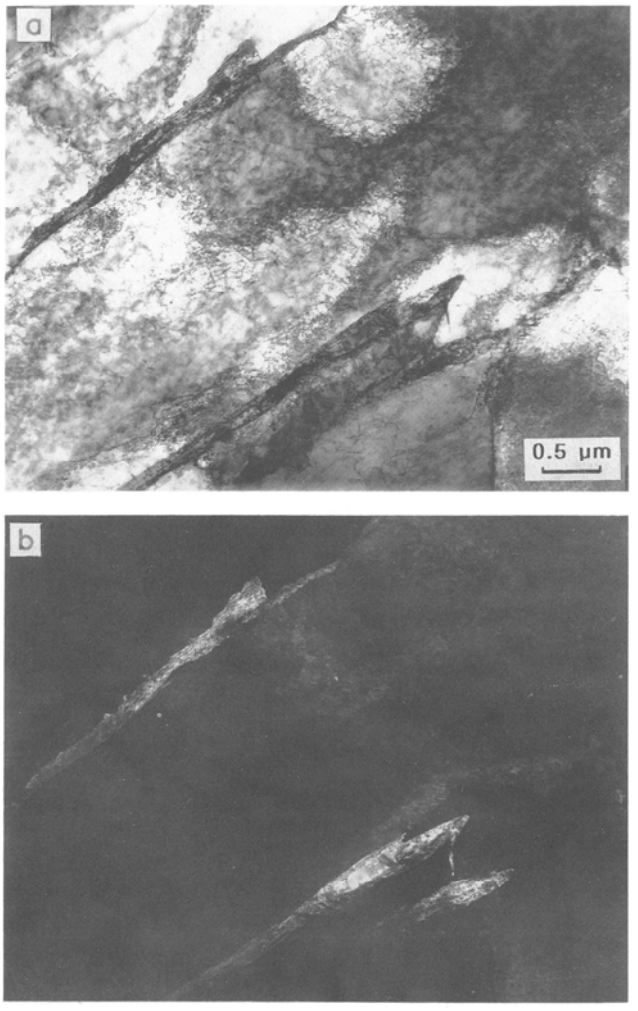

Fig. 12—(*a*) Bright-field and (*b*) dark-field transmission electron micrographs of the simulated ICRCG HAZ, clearly showing the typical dislocated martensite with interlath retained austenite.

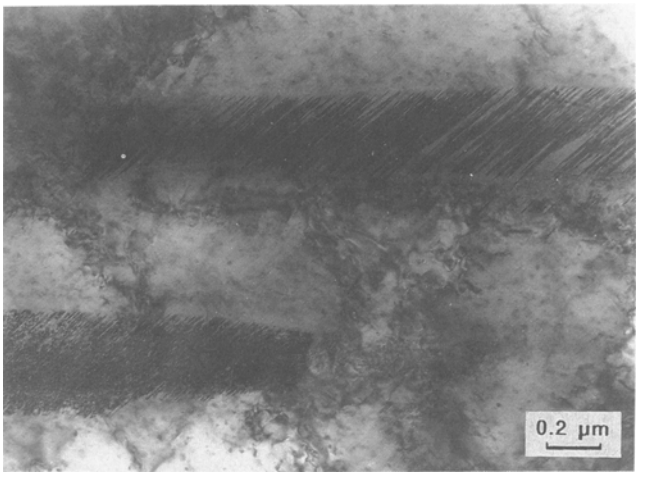

Fig. 13—Transmission electron micrograph of the simulated ICRCG HAZ, showing the typical twinned martensite.

is varied between 800 °C and 1200 °C, the amount of martensitic islands shows a minimum at the T_p^2 of 1000 °C. The highest percentage of martensitic islands in the coarse-grained HAZ corresponds to the minimum in the Charpy energy curve, as shown in Figure 7. This shows the importance of the volume fraction of martensitic islands in the analysis of the Charpy toughness data.

C. *Fractography*

The fracture surfaces of Charpy impact specimens and circumferentially notched tensile specimens were examined to define the nature of the fracture surfaces. Figures 14(a) through (d) are typical SEM fractographs of both test specimens observed in ICRCG HAZ microstructures. At the temperature of −80 °C, fracture surfaces are characterized by cleavage facets, whereas the features observed in specimens tested at −10 °C are fully fibrous. Energy-dispersive spectroscopy analyses of particles found on the fracture surface confirmed that some of the particles responsible for voids were small MnS particles, as shown in Figures 14(c) and (d). These fractographic results, in fact, correlate with the trends in toughness values. The transition from cleavage to fibrous fracture and from lower shelf to upper shelf toughness values with increasing test temperature occurs. It is also noteworthy that the cleavage facet sizes are shifted to larger sizes for the coarse-grained microstructures as compared with the fine-grained microstructures (Figure 15). Examples of cleavage facet size distribution in the simulated HAZ subjected to the thermal cycle of T_p^1 = 1350 °C and 1100 °C are shown in Figure 16. The average sizes were computed to be 53 μm for the structure of T_p^1 = 1350 °C and 35 μm for the T_p^1 = 1100 °C. It has been found by Couque *et al.*[20] that when the fracture mode is cleavage fracture, the measured cleavage facet sizes of a plain carbon steel correlate well with the measured grain sizes of prior austenite. For the simulated HAZ microstructures, the measured cleavage facet sizes are quite consistent with the prior austenite grain sizes (Table II).

D. *Micromechanical Fracture Processes*

To identify the micromechanical fracture processes involved in void and cleavage microcrack initiation, the results of tensile tests and subsequent metallographic studies of the circumferentially notched specimens subjected to the thermal cycles of the ICRCG HAZ were analyzed. Figures 17(a) through (e) show a series of the microstructures beneath the fracture surfaces of the tensile specimens fractured at −10 °C. Voids nucleate by the decohesion of the martensitic islands from the matrix ferrite at the interface of ferrite and stringer-type martensitic islands which are roughly parallel to the tensile axis. Once nucleated, voids grow mainly along the interfaces in the direction of the tensile axis. Figures 17(b) and (c) illustrate how growing cavities interact to form large voids and finally martensitic islands break in the later stage of void growth because of the considerable amount of plastic deformation in the ferrite matrix. These voids have a tendency to be 40 ~ 50 deg apart from the tensile axis when the martensitic islands were approximately parallel to the tensile axis. When the test temperature was lowered to −60 °C, a few microvoids were

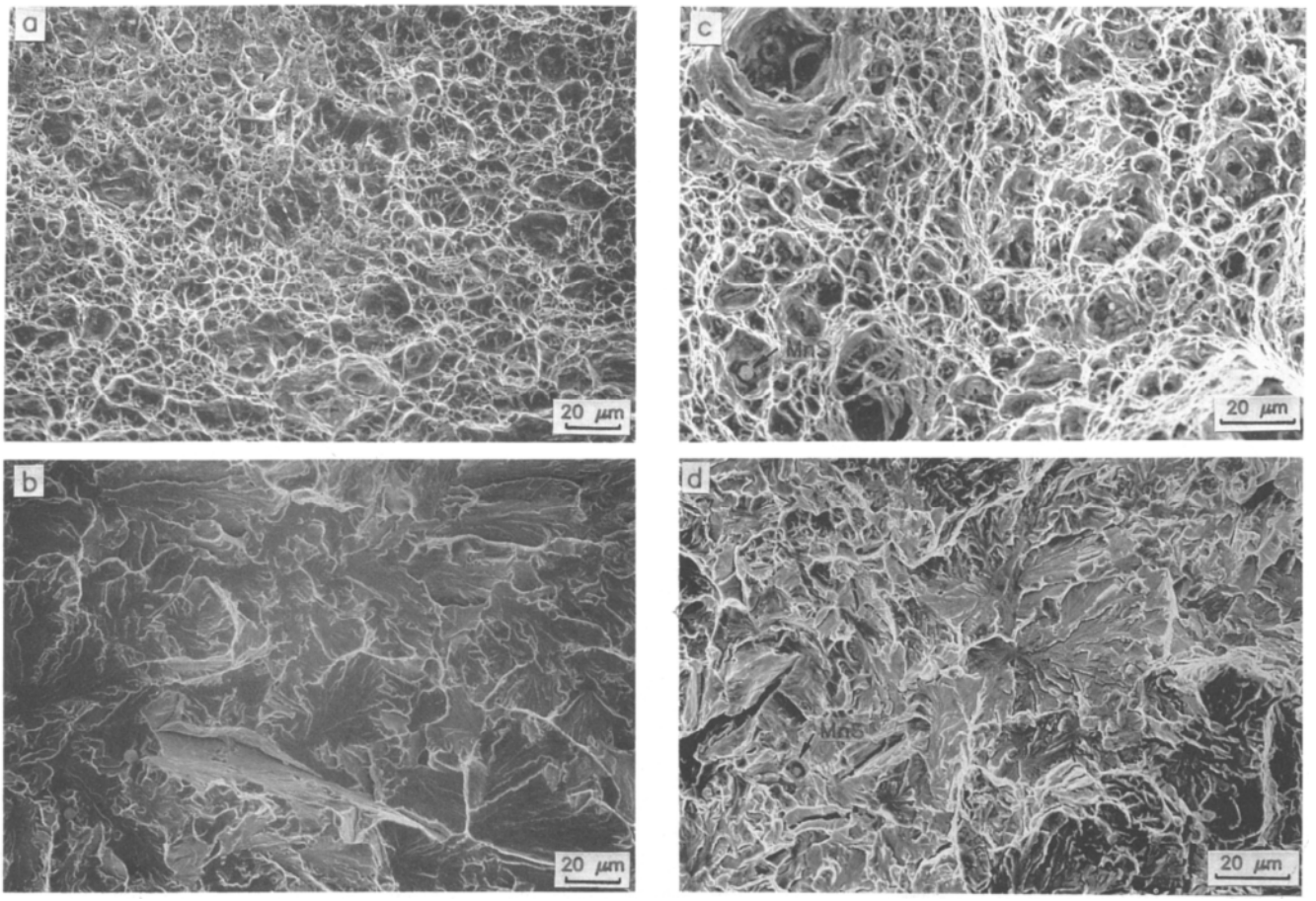

Fig. 14—Scanning electron fractographs of the simulated ICRCG HAZ for Charpy impact specimens fractured at (*a*) −10 °C and (*b*) −60 °C and for notched round specimens fractured at (*c*) −10 °C and (*d*) −60 °C. MnS inclusions are found inside large dimples, as shown in (a) and (c).

observed at the ferrite-martensite interfaces, as shown in Figure 18(a). At the test temperature of −80 °C, a number of microcracks are found beneath the fracture surface instead of microvoids (Figure 18(b)). It is reasonable to assume that the majority of microcracks nucleated from

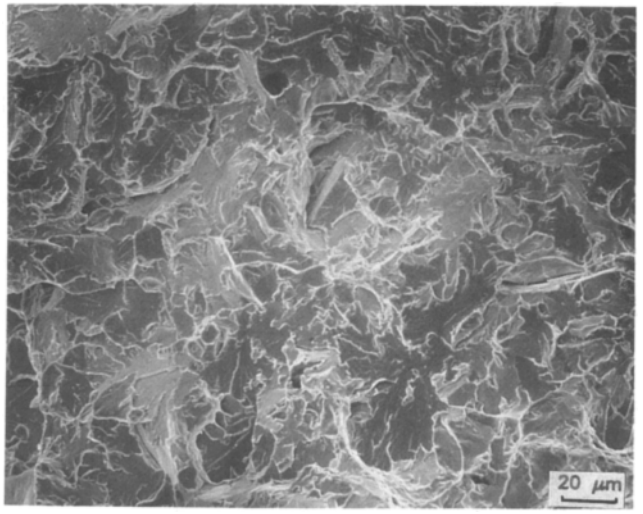

Fig. 15—Scanning electron fractograph of the simulated HAZ (T_p^1 = 1100 °C) for Charpy impact specimens fractured at −60 °C.

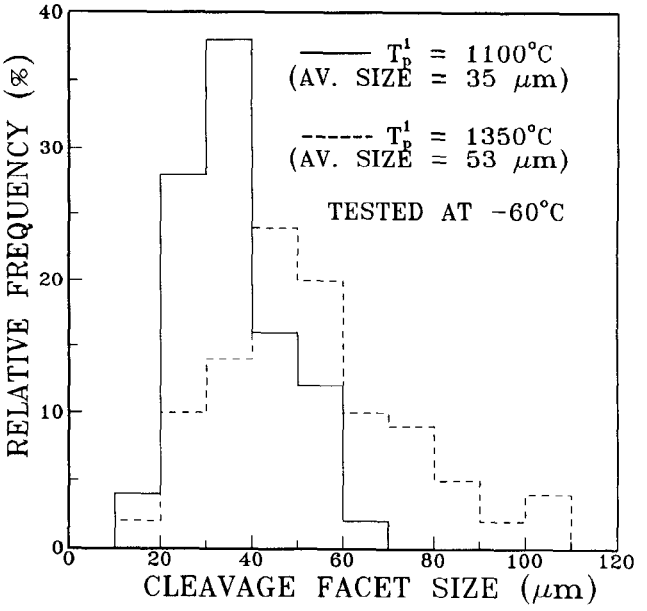

Fig. 16—Relative frequencies of cleavage facet size for Charpy impact specimens subjected to the thermal cycles of T_p^1 = 1350 °C (dashed line) and T_p^1 = 1100 °C (solid line).

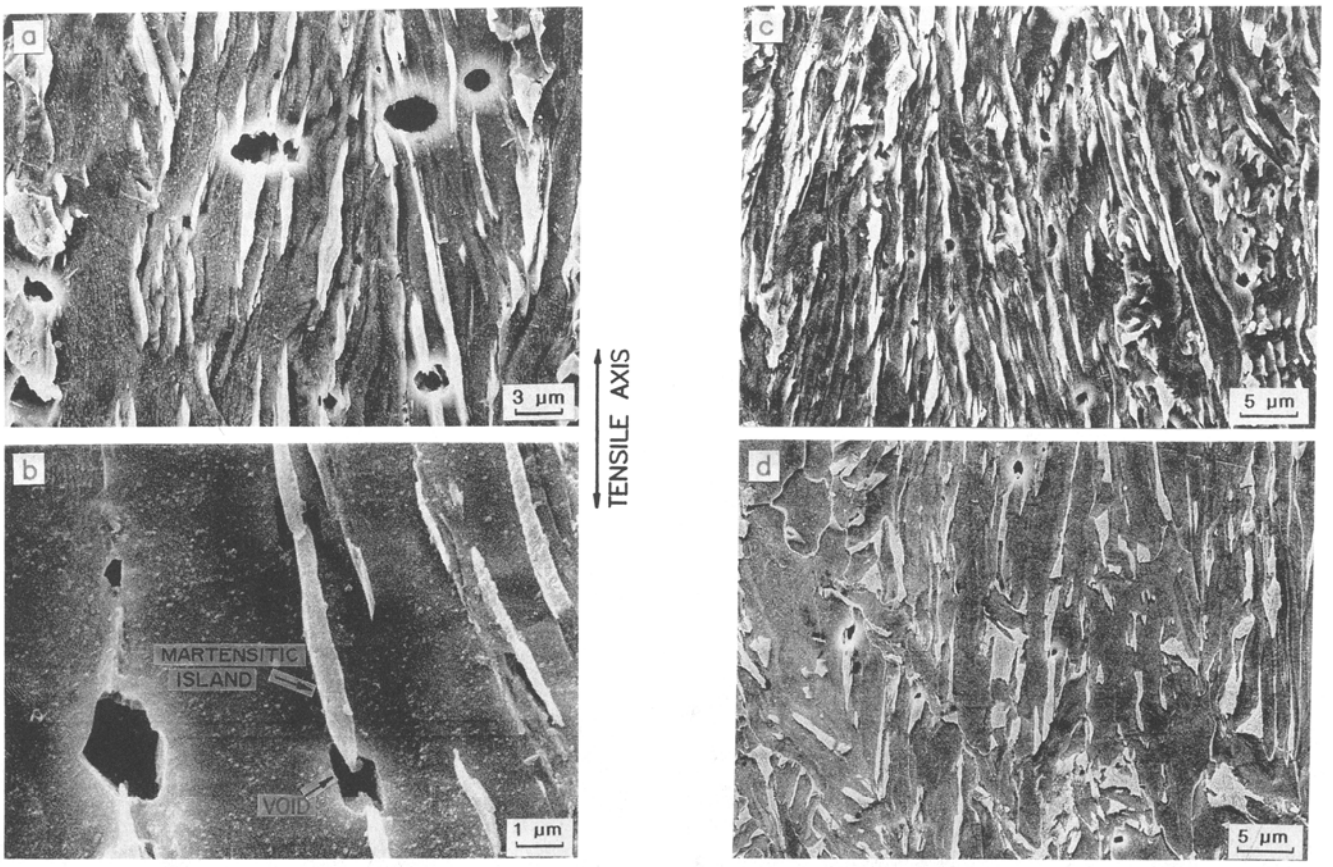

Fig. 17—Scanning electron micrographs of notched round tensile specimens sectioned parallel to the tensile axis, showing the microstructure beneath the fracture surfaces of the simulated ICRCG HAZ fractured at −10 °C. The strain ε_z, which is an appropriate parameter to relate to the average damage in the interior of the specimen, is varied: (*a*) and (*b*) $\varepsilon_z = \varepsilon_f = 0.76$, (*c*) $\varepsilon_z = 0.74$, and (*d*) $\varepsilon_z = 0.69$. The tensile axis is vertical for the micrographs.

the microvoid, considering the observation of microvoids at the temperature of −60 °C. A detailed description of this point will be made later.

IV. DISCUSSION

The purpose of this section is to obtain a valuable insight into the details of the fracture process in HSLA steel welds as it occurs on microscale. Since the analysis of these fracture processes is complicated by several factors such as weld thermal cycle, test temperature, and microstructure, the variation of the Charpy impact energy with the microstructure must be considered in detail.

A useful starting point for interpreting the fracture results in the coarse-grained HAZ, which contained considerable amounts of martensitic islands, is the identification of the micromechanism of fracture processes involved in the initiation of microvoids or microcracks. As mentioned earlier in the section of fracture processes, in the case of ductile fracture, small microvoids which are nucleated initially at the interface between martensitic islands and the ferrite matrix promote shearing of the matrix on the slip plane when the specimen is under tensile stresses. The fine cementite particles play a relatively minor role in controlling the fracture mechanism of the HSLA steel HAZ. It is interesting to note that microvoids were easily formed from the interface of the stringer-type martensitic islands with the orientation 40 ~ 50 deg to the tensile axis when the martensitic island stringers were approximately parallel to the tensile axis, as shown in Figures 17(a) through (f). Conversely, few microvoids were observed when the stringer-type martensitic islands were aligned normal to the tensile axis. This type of microvoid formation at martensitic islands can be explained by the "shear cracking process" described for pearlite colonies by Miller and Smith[21] and subsequently quoted by many other researchers.[20,22,23] The initial microvoids become larger along the interfaces as the surrounding ferrite matrix undergoes plastic deformation and then martensitic islands break in the later stage of void growth. Finally, these growing voids link up to form the dimple pattern in ductile fracture when the shear becomes large enough. The average dimple size of the ICRCG HAZ microstructure is of the order of the measured spacings of martensitic islands associated with voids when the fracture mode is ductile. The average size is computed to be 3.3 μm, which is somewhat larger than the measured spacing of martensitic islands (about 3 μm), but the two sets of sizes overlap within the statistical spread of the size distribution. Thus, the spacing of martensitic islands associated with voids appears to play a strong role in ductile fracture of the coarse-grained HAZ microstructures. A schematic sequence for the ductile void extension described above is illustrated in Figure 19.

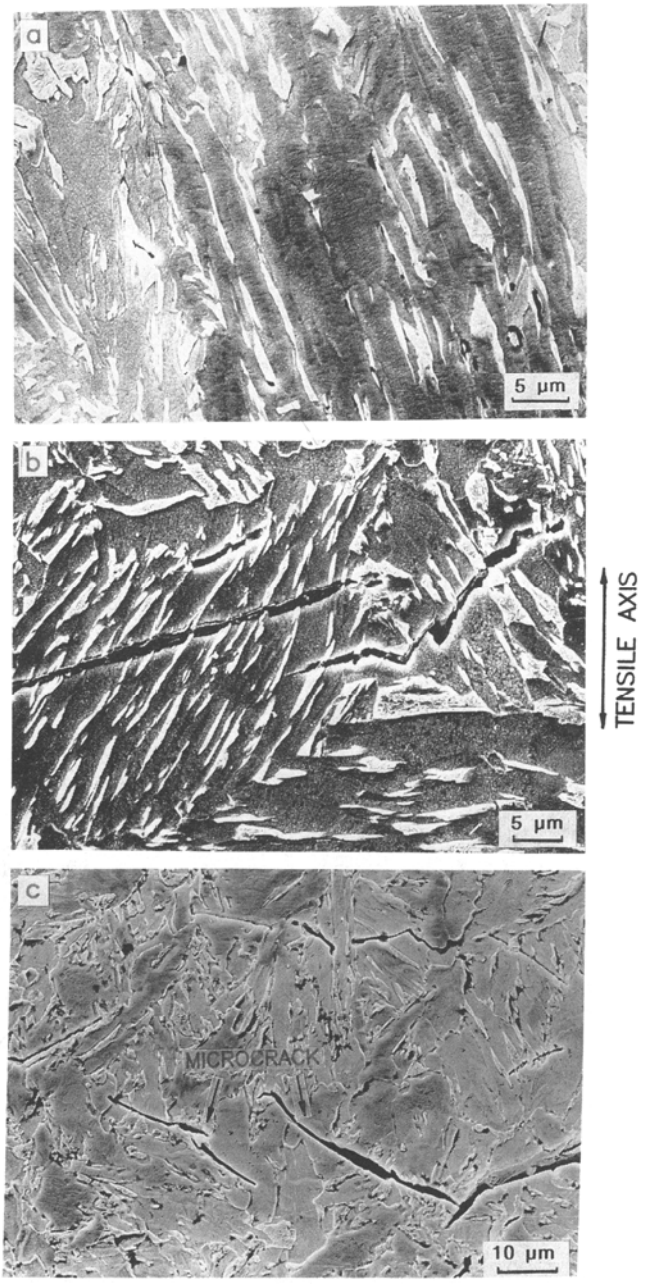

Fig. 18—Scanning electron micrographs of notched round tensile specimens sectioned parallel to the tensile axis, showing the microstructure beneath the fracture surfaces of the simulated ICRCG HAZ fractured at (*a*) −60 °C, (*b*) and (*c*) −80 °C. The tensile axis is vertical for the micrographs.

When brittle fracture dominates, metallographic studies of the interrelation of the microstructure with the fracture process (Figures 18(a) and (b)) suggest that the early stage of the microvoid initiation process is similar to that for ductile fracture. In the case where void growth occurs by cleavage, the first microvoid formed at the martensite-ferrite interface propagates catastrophically as a cleavage crack, until the crack reaches the prior austenite grain boundary. Thus, cleavage fracture along a zig-zag path was observed beneath the fracture surface, as shown in Figure 18(c). This crack extension results from linkup of brittle microcracks with shear cracks,

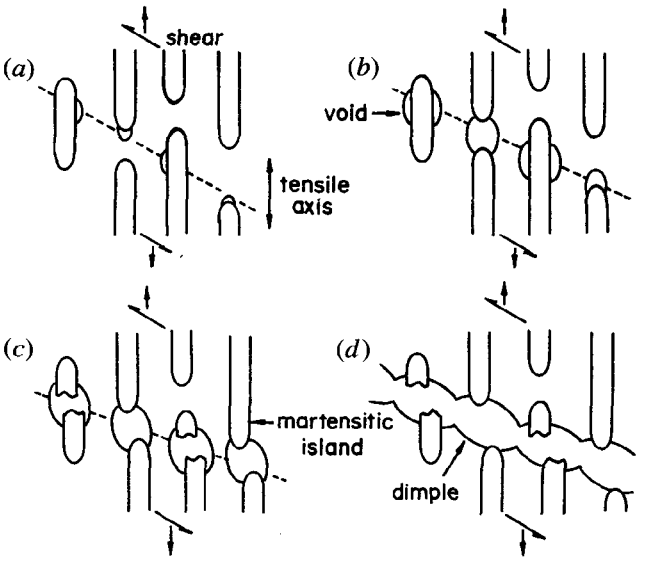

Fig. 19—Schematic illustration of the ductile fracture mechanism in a coarse-grained HAZ of a HSLA steel weld. The cases tested at a temperature above the ductile to brittle transition exhibit ductile rupture.

planes of which are also matched with $\{100\}_\alpha$ ferrite cleavage planes. The fracture process can be described with the sequence schematically illustrated in Figure 20.

Many secondary cracks are also found on the cleavage fracture surfaces of notched tensile specimens subjected to thermal cycle for the ICRCG HAZ, as shown in Figure 21. A blocky structure of a few microns size is also observed at the center of a secondary crack and judged as the martensitic island according to the two-stage electrolytic etching. It is believed that a microcrack or a microvoid nucleated at the ferrite matrix very close to the martensite-ferrite interface in the highly strained region propagates along the martensite-ferrite interface in the tensile direction to form a secondary crack, which acts as a Griffith crack. This is followed by cleavage

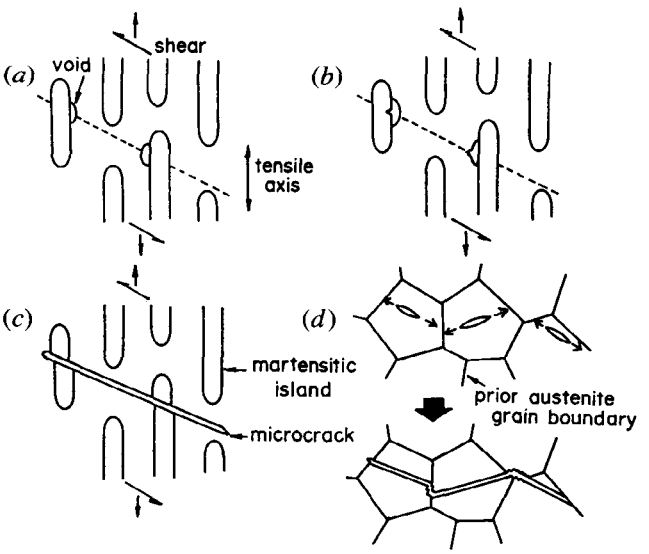

Fig. 20—Schematic illustration of the cleavage fracture mechanism in a coarse-grained HAZ of a HSLA steel weld.

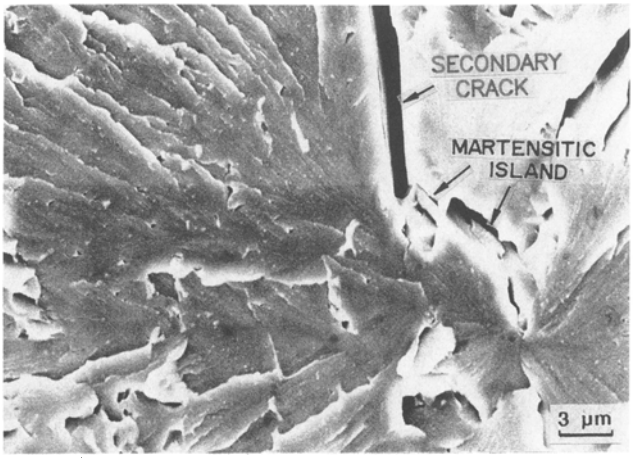

Fig. 21—Scanning electron fractograph of the simulated ICRCG HAZ, showing a cleavage fracture initiation point at the martensitic island inside a second crack.

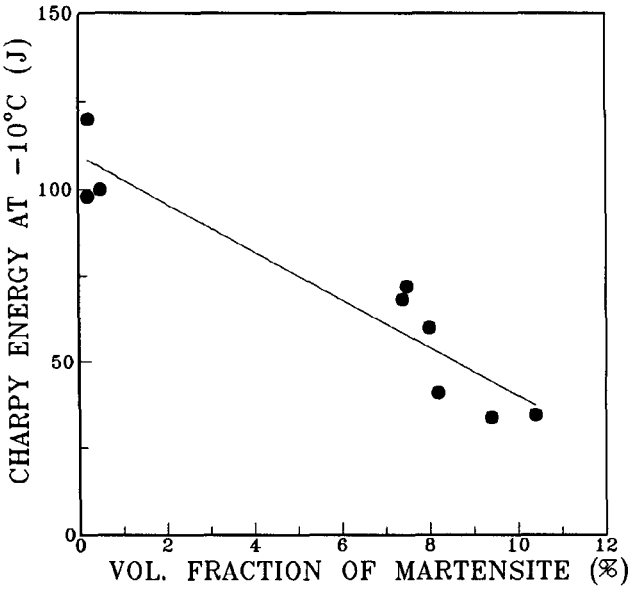

Fig. 22—Relationship between the volume fraction of martensitic islands and Charpy energy.

fracture which is observed to radially propagate from the secondary crack because of stress intensification. This observation seems to support the explanation that the formation of martensitic islands plays an important role in initiating cleavage fracture, thereby reducing the toughness values in the ICRCG HAZ.

It is well known that the effective grain size is an important parameter controlling the Charpy energy. Scanning electron microscopy observations of the cleavage fracture surfaces show that the coarse-grained HAZ structure has a much larger cleavage facet size than the fine-grained HAZ structure (Figures 14(c) and Figure 15). The larger cleavage facet size of the coarse-grained HAZ is associated with the lower Charpy energy. Comparison of the cleavage facet size with the microstructural features shows that the cleavage facet size of the coarse-grained HAZ is of the order of the prior austenite grain size (about 50 μm). Figure 18(b) shows that there is no deflection of the cleavage crack at the ferrite-martensite interfaces; martensite islands do not have any effect in changing the direction of crack propagation.

Kim and Nakagawa[24] have recently investigated microdiffraction patterns of the martensitic islands and ferrite subgrains and have found that both the ferrite and the martensite within a martensite packet have nearly the same crystallographic orientations. The important consequence in terms of brittle fracture is that the entire region within a martensite packet shares the same cleavage plane of ferrite, {100}. In this case, the cleavage crack is not deflected at the ferrite-martensite interfaces. Thus, the effective grain size for cleavage fracture in the simulated HAZ is determined by the prior austenite grain size.

In the context of the present research on the LBZ, we are now able to propose mechanisms for the LBZ phenomena which account for the observed embrittlement fracture mechanism, *i.e.*, initiation of microvoids by the decohesion of interface between the ferrite matrix and martensitic islands. This provides major contribution to LBZ phenomena in microstructures containing larger volume fractions of martensitic islands, leading to cleavage fracture initiation.

We now turn our attention to the relationship of fracture toughness to the microstructures formed in the simulated HAZ. The Charpy energy is well correlated with the effective grain size in the absence of martensitic islands. Figure 6 shows that the impact energy decreases with increasing the T_p^1 as prior austenite grain size is also increased. This transition from high toughness in the fine-grained zone to low toughness in the coarse-grained zone coincides with the change of microstructures including prior austenite grain size, reflecting that the prior austenite grain size was changed from 30 to 49 μm with increasing the first peak temperature. However, in the presence of the martensitic islands, the effect of the grain size on toughness is rather complicated. It should be considered that the Charpy energy drops drastically from 123 to 35 J, whereas grain size is not significantly increased. Thus, grain size is not the dominant factor to influence the fracture mechanism of local embrittlement.

By comparing the amount of martensitic islands and the Charpy energy, one finds that martensitic islands play an important role in reducing the toughness of the coarse-grained HAZ. The drastic decrease in the impact energy value at the ICRCG HAZ zone, as shown in Figure 7, is attributed to the significant increase in the amount of martensite (Table II). It is clear from Figure 22 that the Charpy value decreases linearly with increasing volume fraction of martensite regardless of the type of weld thermal cycles. Therefore, it can be concluded that the initiation of microvoids at the interface between martensitic islands and the ferrite matrix is primarily responsible for the reduction in the Charpy toughness of the coarse-grained HAZ through its effects on interfacial decohesion.

The results indicate that the relationship of the fracture toughness to the microstructures formed in the coarse-grained HAZ of HSLA steel welds is rather complex. Nevertheless, the experimental results described above provide a means of correlating the impact energy with microstructure. Correlation of the weld thermal cycle and

the microstructure is extremely important for the understanding of fracture in the welded joints, but much remains to be learned concerning the actual microfracture processes that occur at a crack tip. In the present investigation, the fracture behavior is evaluated mainly by means of the Charpy test because of its convenience and familiarity. However, Charpy test results are difficult to relate to fracture mechanics concepts and, in particular, to the stress intensity factor, K_I. More fundamental difficulties with the Charpy test lie in the fact that plane strain conditions are not fully met in the specimen. Accordingly, we are currently carrying out J_{Ic} tests in which plane strain conditions are met. Therefore, future studies should include further detailed analyses of fracture processes, such as void initiation and propagation at a sharp crack tip and parallel measurements of toughness properties. It is hoped that the results of this parallel study will provide valuable insights into microscopic mechanisms of fracture in the local brittle zone of HSLA steel welds.

V. CONCLUSIONS

1. Correlation of the microstructure with the fracture behavior was investigated by examining the micromechanism of fracture processes in the LBZ of HSLA steel welds.
2. The coarse-grained HAZ includes two locally brittle microstructures whose toughness values are strongly affected by the amount of martensitic islands.
3. Microvoids are observed to initiate at the interface between martensitic islands and the ferrite matrix by the shear process, *i.e.*, the decohesion of the martensitic islands with the orientation 40 ~ 50 deg to the tensile axis when the martensitic islands are approximately parallel to the tensile axis.
4. The martensitic island is the main metallurgical factor which contributes to local embrittlement in microstructures containing larger volume fractions of martensitic island, leading to cleavage fracture initiation. The effective grain size for cleavage fracture in the simulated HAZ is determined by the prior austenite grain size.

ACKNOWLEDGMENTS

This work was supported by the Research Institute of Industrial Science and Technology (RIST) under Contract No. 8-118-A. Use of the RIST Technical Service Center Facility is gratefully acknowledged. The authors are also thankful to Mr. C.S. Lee and Mr. J.H. Eom for their discussion of this work.

REFERENCES

1. D.P. Fairchild: in *Welding Metallurgy of Structural Steels*, J.Y. Koo, ed., TMS, Denver, CO, 1987, pp. 303-18.
2. J.G. Youn and H.J. Kim: *Proc. 2nd Conf. on Mechanical Behaviors of Materials*, Seoul, Korea, KIM, Seoul, 1988, pp. 35-43.
3. H.G. Pisarski and J. Kudoh: in *Welding Metallurgy of Structural Steels*, J.Y. Koo, ed., TMS, Denver, CO, 1987, pp. 263-75.
4. R. Denys and H.I. McHenry: *Proc. 7th Int. Conf. on Offshore Mechanics and Arctic Engineering*, Houston, TX, ASME, Golden, CO, 1988, pp. 379-85.
5. T. Haze and S. Aihara: *Proc. 7th Int. Conf. on Offshore Mechanics and Arctic Engineering*, Houston, TX, ASME, Golden, CO, 1988, pp. 515-23.
6. K. Uchino and Y. Ohno: *Proc. 7th Int. Conf. on Offshore Mechanics and Arctic Engineering*, Houston, TX, ASME, Golden, CO, 1988, pp. 159-65.
7. K. Satoh and M. Toyoda: *Proc. 7th Int. Conf. on Offshore Mechanics and Arctic Engineering*, Houston, TX, ASME, Golden, CO, 1988, pp. 495-502.
8. G.R. Wang, T.W. Lau, G.C. Weatherly, and T.H. North: *Metall. Trans. A*, 1989, vol. 20A, pp. 2093-2100.
9. J.Y. Koo and A. Ozekcin: in *Welding Metallurgy of Structural Steels*, J.Y. Koo, ed., TMS, Denver, CO, 1987, pp. 119-35.
10. K. Masubuchi: *Analysis of Welded Structures*, Pergamon Press, New York, NY, 1980, ch. 2.
11. The Welding Institute's Engineering Department: *Metal Construction*, May 1982, pp. 272-77.
12. British Standards Institution Document BS 5762, 1979.
13. S. Lee: *Scripta Metall.*, 1988, vol. 22, pp. 59-64.
14. S. Lee, D.Y. Lee, and R.J. Asaro: *Metall. Trans. A*, 1989, vol. 20A, pp. 1089-1103.
15. K. Yoneo and A. Takao: *J. Jpn. Weld. Soc.*, 1981, vol. 50, pp. 19-28.
16. B.C. Kim, J.H. Eom, C.S. Lee, S. Lee, and D.Y. Lee: *J. Korean Weld. Soc.*, 1989, vol. 7, pp. 35-48.
17. T. Haze, S. Aihara, and H. Mabuchi: in *Accelerated Cooling of Rolled Steel*, P.D. Southwick, ed., TMS, Warrendale, PA, 1986, pp. 235-47.
18. S. Dionne, M.R. Krishnadev, L.E. Collins, and J.D. Boyd: in *Accelerated Cooling of Rolled Steel*, P.D. Southwick, ed., TMS, Warrendale, PA, 1986, pp. 71-84.
19. N.J. Kim and G. Thomas: *Metall. Trans. A*, 1981, vol. 12A, pp. 483-89.
20. H. Couque, R.J. Asaro, J. Duffy, and S.H. Lee: *Metall. Trans. A*, 1988, vol. 19A, pp. 2179-2206.
21. L.E. Miller and G.C. Smith: *J. Iron Steel Inst.*, 1970, vol. 208, pp. 998-1005.
22. K. Park and I.M. Bernstein: *Metall. Trans. A*, 1979, vol. 10A, pp. 1653-64.
23. K. Nakase and I.M. Bernstein: *Metall. Trans. A*, 1988, vol. 19A, pp. 2819-29.
24. N.J. Kim and A.H. Nakagawa: *Mater. Sci. Eng.*, 1986, vol. 83, pp. 145-49.